Article

Mesoporous Few-layer Graphene Platform for Affinity Biosensing Application

Md. Azahar Ali, Chandan Singh, Kunal Mondal, Saurabh Srivastava, Ashutosh Sharma, and Bansi Dhar Malhotra

ACS Appl. Mater. Interfaces, **Just Accepted Manuscript** • DOI: 10.1021/acsami.5b12460 • Publication Date (Web): 07 Mar 2016

Mesoporous Few-layer Graphene Platform for Affinity Biosensing Application

Md. Azahar Ali[1], Chandan Singh[2], Kunal Mondal[1], Saurabh Srivastava[3], Ashutosh Sharma[1]*, Bansi D. Malhotra[3#]
[1]Department of Chemical Engineering, Indian Institute of Technology Kanpur, Kanpur-208016, India
[2]Department of Science and Technology Centre on Biomolecular Electronics, Biomedical Instrumentation Section, CSIR-National Physical Laboratory, Dr. K. S. Krishnan Marg, New Delhi-110012, India
[3]Department of Biotechnology, Delhi Technological University, Shahbad Daulatpur, Main Bawana Road, Delhi-110042, India

ABSTRACT

A label-free, highly reproducible, sensitive and selective biosensor is proposed using anti-apolipoprotein B 100 (AAB) functionalized mesoporous few-layer reduced graphene oxide and nickel oxide (rGO-NiO) nanocomposite for detection of low density lipoprotein (LDL) molecules. The mesoporous rGO-NiO composite formation on indium tin oxide conductive electrode has been accomplished *via* electrophoretic technique using colloidal suspension of rGO sheets and NiO nanoparticles. This biosensor shows good stability obtained by surface conjugation of antibody AAB molecules with rGO-NiO matrix by EDC-NHS coupling chemistry. The defect-less few layer rGO sheets, NiO nanoparticles (nNiO) and formation of nanocomposite has been confirmed by Raman mapping, electron microscopic studies, X-ray diffraction and electrochemical techniques. The synthesized rGO-NiO composite is mesoporous dominated with a small percentage of micro and macroporous structure as is evident by the results of Brunauer–Emmett–Teller experiment. Further, the bio-conjugation of AAB with rGO-NiO has been investigated by Fourier transform-infrared spectroscopy studies. The kinetic studies for binding of antigen-antibody (LDL-AAB) and analytical performance of this biosensor have been evaluated by impedance method. This biosensor exhibits an excellent sensitivity of 510 Ω $(mg/dL)^{-1}$ cm^{-2} for detection of LDL molecules. This biosensor is sensitive to 5 mg/dL concentration of LDL in a wide range of 0-130 mg/dL. Thus, this fabricated biosensor is an efficient and highly sensitive platform for the analysis of other antigen-antibody interactions and biomolecules detection.

Keywords: Label-free, Impedance spectroscopy, Mesoporosity, Reduce graphene oxide, Nickel oxide nanoparticles, Low density lipoprotein

1. INTRODUCTION

There is increased interest towards the search of new smart nanomaterials including those based on graphene for biomedical applications[1]. The reduced graphene oxide (rGO), owing to its interesting electrochemical, electronic and functional properties, has been found to have a wide range of applications including field effect transistors, nanoelectronic devices and point-of-care biosensors.[2-7] Extremely high specific surface area of rGO and its reduced functional groups can be advantageous for enhancing the loading of biomolecules (DNA, sRNA, antibody, proteins etc.)[8] indicating it as an excellent candidate for development of electrochemical biosensors.[7] The transition from insulating GO to semiconductor rGO can be accomplished *via* chemical or thermal process resulting in increased electrical conductivity over several orders of magnitude. The rGO bears definite amount (8 atomic percent) of residual oxygen bonded with approximately 20% sp^3 hybridized carbon atoms allowing the possibility of chemical bonding with biomolecules using covalent coupling such as amide linkage.[9]

The reduction of functional groups (-COOH, -OH, and -CHO) at GO is directly linked with the electronic properties such as electrical conductivity and mobility of electrons due to increased sp^2 fraction that may lead to improved sensitivity and response time of a biosensor.[10-12] Zhou *et al.* fabricated an electrochemical biosensor based on rGO conjugated with glucose oxidase and alcohol dehydrogenase wherein rGO sheets and found greater electrocatalytic activity for hydrogen peroxide and β-nicotinamide adenine dinucleotide.[13] Jung *et al.* reported a GO based immuno-biosensor for detection rotavirus using fluorescence resonance energy transfer between GO sheets and gold nanoparticles for the development of point-of-care biosensor.[14] Though the available functional groups in rGO may facilitate conjugation of biomolecules, the electrochemical conductivity is currently a limitation for development of

efficient biosensors.[14] To solve this problem, rGO can be electrophoretically deposited with nanostructured metal oxides (NMOs) wherein the NMOs can be used to obtain the improved electrochemical reactivity.[15-19] The NMOs encapsulated rGO sheets can be stabilized *via* mutual electrostatic interactions between negatively charged graphene layer and the positively charged NMOs resulting in uniform thin film of rGO sheets.[20] This unique nanohybrid structure may offer several advantages such as reduced agglomeration of oxide nanoparticles and higher electrical conductivity.[15]

There is a significant interest in the development of multifunctional materials for fabrication of point-of-care devices.[21-26] Depending on the type of application, many nanomaterials including those of metals, polymers and metal oxides have been incorporated in rGO sheets. The application of rGO-NMOs in biosensors, solar cells, photocatalysis, electrochemical is widely explored due to its synergistic effect.[27, 28] The NMOs can perhaps be distributed on rGO surface or between the rGO layers leading to new nanocomposites with enhanced mechanical, catalytic, and electrochemical properties.[29-31] For example, TiO_2–graphene composite was used for hydrogen evolution from water photocatalytic splitting while the SnO_2-graphene was utilized for highly improved cycling process and lithium storage.[32, 33] NMOs can act as spacer preventing restacking of the rGO sheets and the pseudocapacitance of these NMOs combined with the double layer capacitance of rGO may enable fast and reversible reactions for electrochemical applications[16-19]. Song *et al.* have fabricated a non-enzymatic glucose biosensor based on CuO/graphene composite wherein sensitivity and limit of detection of this biosensor has been improved.[34] The application of TiO_2/graphene nanohybrid was reported for rapid detection of acetylcholinesterase and glucose.[35, 36] And the nanostructured nickel oxide (nNiO) has been explored for composite formation with rGO sheets in order to improve the biosensing characteristics. Recently, nanoparticles, nanorods and hollow spheres of NiO were employed for

electrochemical biosensing and energy storage.[37, 38] The rod-shaped NiO was found to be an excellent material due to its environmental stability and its characteristic not to degrade on immobilization of biomolecules, make it an important material for biosensor.[39, 40] The binding of biomolecules on nNiO is important for obtaining enhanced sensitivity, limit of detection and response time. The integration of nNiO with rGO sheets may provide an interesting interface for effective carrier transport with significantly reduced carrier scattering. With dominant mesoporous feature of rGO-NiO composite and due to its large pore volume, it can used for holding antibody molecules with increased loading capacity. The enhanced loading of biomolecules can directly influence the sensitivity by binding increased number of target molecules and holding of the antibodies into the pores may result in enhanced stability of a biosensor. In addition to this, rGO-NiO offers highly balance electron and hole mobility resulting into the superior performance for the biosensing application.[41] The rGO may facilitate wrapping of nNiO leading to the formation of smooth and uniform film that offers a suitable surface for the antibody attachment.[20] With these properties, the mesoporous functional rGO-NiO composite is a new platform for real time monitoring of lipid molecules in human blood samples.

We demonstrate the fabrication of a label-free, sensitive immunosensor using a mesoporous rGO-NiO composite. The surface immobilization of bovine serum albumin (BSA) and anti-apolipoprotein B 100 (AAB) on the surface of rGO-NiO composite was conducted by conjugation EDC-NHS coupling chemistry. The mesoporosity, morphological shape, size, and distribution of nNiO on rGO sheets were confirmed by Brunauer–Emmett–Teller (BET) and electron microscopic studies. The rGO-NiO based immunosensor has been utilized for the detection of low density lipoprotein (LDL) molecules in human serum samples by electrochemical impedance technique.

2. EXPERIMENTAL SECTION

2.1 Chemicals. Graphite powder flakes (99.99, wt%) were procured from Aldrich Sigma, USA. Low density lipoprotein (MW: 3500 kDa), anti-apolipoprotein B 100 (MW: 515 kDa), bovine serum albumin (BSA), N-hydroxysuccinimide (NHS) and N-ethyl-N0-(3-dimethylaminopropyl carbodiimide) (EDC) were purchased from Sigma Aldrich, USA. Di-ionized water was from Millipore water purification system. 5 mg of lyophilized powder of LDL was mixed with 1 mL deionized water containing 150 mM NaCl of pH 7.4 and 0.01% EDTA. Solution of BSA (2 mg/mL) was prepared in 50 mM phosphate buffered saline (PBS) of pH 7.4 containing 150 mM NaCl. Anti-apolipoprotein B 100 (AAB) solution (1 mg/mL) was prepared in PBS (50 mM) solution of pH 7.4 containing NaCl (150 mM).

2.2 Electrode fabrication. The rGO was synthesized using modified Hummer's method as reported in literature.[42] The $Ni(OH)_2$ nanorods powder was synthesized using chemical route and annealed at 700 °C to form nanostructured NiO.[43] The chemically synthesized rGO-NiO nanocomposite was deposited onto indium tin oxide (ITO) coated glass substrate *via* electrophoretic deposition (EPD) technique.[42] We first prepared well-dispersed colloidal solutions of NiO nanorods (0.6 mg/mL) and rGO (5 mg/dL) in acetonitrile by ultrasonication (40W, 0.25 A) for about 4 h. For EPD, 300 µL of this stock solution of rGO sheets and 300 µL of nNiO were dispersed in 10 mL of acetonitrile and sonicated for 30 min to form colloidal suspension. Then, this mixture suspension was used for EPD in a two electrodes glass cell. To obtain surface charge on the NiO modified rGO sheets, 10^{-5}–10^{-4} mol of $Mg(NO_3)_2.6H_2O$ was added into the suspension as an electrolyte during EPD. The Mg^{2+} ions adsorbed by rGO sheets provided an adequate positive surface charge resulting in enhanced deposition rate at the anode

(ITO) while platinum acted as cathode. On application of electric field (potential: 67 V for 5 min), the positively charged nNiO were grafted to negatively charged rGO sheets *via* electrostatic interaction and at same time these nNiO grafted rGO sheets were deposited onto ITO substrate (size: 0.25 cm^2 sheet resistance; 30 Ω cm^{-1}). We investigated the surface electrokinetic potential using zeta potential studies for nNiO, rGO sheets and rGO-NiO in acetonitrile solvent. The zeta potential was obtained as +10.0 mV for nNiO dispersed in solution indicating that these were positively charged (Fig. S1 a, Supporting Information). The negative zeta potential (-19.4 mV) of rGO sheets, indicating that presence of the various negatively charged groups on the basal and edge plane offered strong electrostatic interactions with positively changed nNiO (Fig. S1, b). After nNiO incorporation, the zeta potential of rGO sheets was decreased to -14.5mV (Fig. S3, c). With Mg^{2+} ions, the negatively charged rGO-NiO sheets were uniformly deposited on ITO electrode on application of applied voltage. Subsequently, the fabricated electrode (rGO-NiO/ITO) was removed from the cell and washed with de-ionized water followed by drying at 100^{o}C.

2.3 Preparation of biosensor. Schematic 1 shows the fabrication of a biosensor and antibody immobilization on the surface of rGO-NiO electrode for detection of LDL molecules. For antibody immobilization, 20 µL of AAB solution was uniformly spread on the rGO-NiO electrode surface and kept in a humid chamber for about 6 h and subsequently stored at 4°C. The covalent bond formed between -COOH groups of the rGO-NiO sheets and the $–NH_2$ groups of AAB *via* strong amide bond (CO-NH). The surface of rGO-NiO electrode was used to treat EDC-NHS solution in which EDC (0.2M) worked as a coupling agent and NHS (0.05M) worked as an activator. The EDC-NHS coupling chemistry was utilized for the activation of –COOH groups on rGO sheets. BSA was spread on the surface of AAB/rGO-NiO to block the non-

specific active sites on electrode. The BSA-AAB/rGO-NiO immunoelectrode was then washed with phosphate buffered saline (PBS) and stored at 4ºC, when not in use.

3. RESULTS AND DISCUSSION

3.1 Brunauer–Emmett–Teller analysis. Brunauer–Emmett–Teller (BET) analysis was performed for rGO-NiO powder to measure its specific surface area. The rGO-NiO matrix exhibits a specific surface area of 134.3 m^2/g. The nitrogen adsorption-desorption isotherm and pore size distribution of rGO-NiO are shown in Figure 1a. The results of BET studies (Table S1) show calculated total pore volume of micro, meso and macropores distributed with total pore volume of about 0.3383 cc/g. The pore size distribution shown in the inset of Figure 1a shows that the rGO-NiO is found to be mesopores dominated with a small percentage of micro and macropores. The average specific pore size calculated by the Barrett-Joyner-Halenda (BJH) method is about 10.08 nm that supports the pore size distribution curve. This porous structure may be due to the high surface area of the rGO-NiO. The high BET surface area of this mesoporous structure and accessible pore volume help towards efficient attachment of the reactant species on electrode for improved electrochemical activity. Decoration of the mesoporous structure with small percentage of micro and macropores connected to the external particle surface of rGO-NiO with several functional groups are beneficial for controlled release/delivery and biosensing application.

3.2 Raman spectroscopic studies. Raman spectroscopy is a non-destructive tool that can be used to investigate the ratio of sp^2/sp^3 bonding, layers of graphene sheets and study of the nature of sp^2 domains of graphene derivatives. Raman studies were conducted for nNiO and rGO-NiO at 25 ºC as shown in Figure 2b. The Raman peak at 484 cm^{-1} of nNiO is due to one phonon (1P)

transverse optical (TO) mode (curve i) that confirms the existence of nNiO in the sample (curve i). Another peak at ~1090 cm^{-1} is due to two-phonon 2LO (longitudinal optical) mode. The spectra for rGO-NiO (curve ii) shows two distinct peaks at 1344 cm^{-1} and 1581 cm^{-1} are as attributed to disorder (D-band) and graphitic (G-band). The D-band is associated with defects, vacancies and distortions which measure the sp^3 bonding in rGO sheets while G-band linked with the sp^2-hybridized carbon-carbon bond arises due to first order scattering of E_2g mode.[44] The intensity of D-band is 200 times less as compared to that of G-band indicating less defect content in rGO sample. The intensity ratio (I_D/I_G) of the prepared rGO-NiO composite calculated as 0.66 and is mainly due to existence of the unrepaired defects that are present after the elimination of oxygen moieties from reduced GO. A broad and intense peak seen at 2707 cm^{-1} (called 2D-band) corresponds to the double-resonance process due to two-phonon intra-valley scattering whose intensity is much less as compared to G peak of the bulk graphene. The presence of 2D-peak reveals that the prepared rGO is multilayered. The ratio of I_{2D}/I_G found to be as 0.73 may be attributed to recovering of sp^2 C-C bonds (graphitization) in graphitic structure. The average crystallite size was calculated as 12.6 nm using Eq.1.

$$L_a(\mathrm{nm}) = (2.4 \times 10^{-10})\lambda_l^4 \left(\frac{I_D}{I_G}\right)^{-1} \quad (1)$$

where λ_l is the wavelength of the laser in nm, while I_D and I_G are the intensities of D and G bands, respectively.[45] The number of atomic layers of rGO sheet can be correlated with the peak position of G-band in the rGO spectra using the relation[46]

$$\omega_G = 1581.6 + 11/(1 + n^{1.6}) \quad (2)$$

where, ω_G is the band position in wavenumbers, and n is the number of layers present in the sample. It has been found that the layers of thus synthesized rGO are about 4. The intensity maps

of the 'D', 'G' and '2D' bands have been shown in Figure 2(a, b), respectively. Image (a) shows optical mapping of the various peaks present in the rGO-NiO composite. In image (b), the bands ('D', 'G' and '2D') found for rGO-NiO composite can be distinguished by individual colour difference. The presence of G-, D-, and 2D- peaks indicates blue, green and sky colours, while nNiO refers to the red colour. The intensity for G-peak is found to be low and is shown by red circle. The low intensity for red colour mapping is overlapped with green colour indicating nNiO. In the intensity map a large amount of sky and blue colour are seen and overlapped each other as is evident by Raman spectra. 2D and 3D optical profilometric images are shown in Figure 2(c and d) in order to confirm the thickness of the rGO-NiO matrix deposited onto ITO electrode. Figure 2(c and d) clearly shows that rGO sheets are interconnected with each other on ITO surface. The average thickness of deposited rGO-NiO is estimated as 281 nm (Fig. S2, Supporting Information).

3.3 FT-IR studies. Fourier transform infrared (FT-IR) studies confirm the immobilization of antibody on rGO-NiO film (Fig. 1c). The infrared peak found at 538 cm^{-1} in both spectra corresponds to vibration bending of Ni-O. The absorption bands seen at ~1000–2500 cm^{-1} correspond to the O–C=O symmetric and asymmetric stretching, and C–O stretching vibrations due to adsorption of CO_2. The absorption peaks found at 1714 and 1400 cm^{-1} may be responsible for C=O stretching and N-H (amide) bending of carboxyl groups in rGO, respectively (spectra i). The peak at 1585 cm^{-1} is due to N-H stretching while the peak observed at 1245 cm^{-1} is due to C-N (amine) stretching vibration. A peak observed at 2177 cm^{-1} is due to C≡C stretching. Some additional peaks seen at 3349 and 3757 cm^{-1} are due to presence of amide A and amide II (overlapping with O-H stretch). The peak observed at 2843 cm^{-1} is assigned to C-H stretching. The intense peaks observed at 3531 and 3775 cm^{-1} are due to amide II and O-H starching at antibody immobilized rGO-NiO surface (spectra ii). Srivastava *et al.* explained that the

carboxylic (-COOH) groups at rGO can be utilized to bind with $–NH_2$ groups of the antibodies and confirmed by X-ray photoelectron spectroscopy.[42]

3.4 X – Ray diffraction studies. X-ray diffraction (XRD) studies (Fig. 1d) were used to investigate the crystalline structure of rGO (i) and rGO-NiO (ii). A broad peak appears at 2θ position of 25.7º due to (002) reflection plane that indicates presence of rGO. The interlayer spacing of rGO is estimated to be as 0.68 nm (FWHM=12.2º) for the crystallographic plane (002) using Debye-Scherrer Eq.2

$$d_{002} = \frac{0.9\lambda}{\beta_{002}\cos\theta_{002}} \quad (2)$$

where β_{002} is the full width at half maximum (FWHM) and d_{002} is the interlayer spacing. The interlayer spacing of rGO is higher than that of pristine graphite (0.34 nm) due to the available oxygen functional groups at rGO sheets. In the XRD pattern (ii), the different crystallographic planes such as (111), (200), (220), (311) and (222) confirm the formation of nNiO [JCPDS Card No. 78-0423]. The relative peak for plane (200) is found to be dominant. The intensity ratio between two planes (111) and (200) of nNiO is calculated as 0.71, which is much lower than that of bulk NiO (1.45), indicating preferred crystallization along the plane (200). The curve (ii) shows the presence of all crystallographic planes that are observed separately in both synthesized materials. These results confirm the graftation of nNiO with rGO sheets.

3.5 UV-visible spectroscopic studies. To confirm the electronic structure of the synthesized rGO (a) and nNiO (b) and rGO-NiO (c), UV-visible studies were conducted using a source having slit width of 2 nm (Fig. S3, Supporting Information). The absorption is found to increase from 400 nm and the maximum absorption seen at 266 nm is due to π-π* transition of aromatic C-C bonds of rGO. Srivastava *et al.* have shown that reduction of the functional groups in rGO

results in improved electronic behaviour compared to graphene oxide (GO).[42] The band gap of rGO is calculated to be as ~3.0 eV by Tauc equation which is lower as compared to GO (4.0 eV). The maximum absorption peak in nNiO (curve b) observed at 316 nm is due to intra-3d transition of Ni^{++} in the cubic structure of nNiO. An intense peak observed for rGO-NiO at 254 nm and blue shift from rGO absorption peak reveals the formation of rGO-NiO composite. This phenomenon perhaps occurs due to close conjugation of the rGO and nNiO resulting into the rapid electron transfer and increased transition energy as reported in literature.[47] The observed increase in absorption intensity for the rGO-NiO composite can be attributed to electronic coupling of electronic states between NiO and rGO.[47]

3.6 Microscopic studies. The shape, size and structure of synthesized nNiO, rGO sheets and rGO-NiO were observed (Fig. 3) by field emission-scanning electron microscopy (FE-SEM). Image (a and b) shows that the NiO has elongated hexagonal structure (Fig. 3). The elongated NiO molecules appear to form nanorods structure having size less than 200 nm. Some of the NiO nanoparticles appear to be hexagonal. Image (c and d) shows overview of the rGO sheets that are deposited on ITO electrode (Fig. 3). It is clear that these rGO flakes are folded and wrinkled, and agglomerated flakes are stacked due to π-π interactions among the individual sheets with lateral sizes ranging from nanometers to microns. A clear and high magnification image (e) shows the edges and basal planes of rGO sheets. The higher magnification was used to distinguish the individual rGO sheets (image e). Image (f and g) shows distribution of the NiO nanorods on rGO sheets. The rGO sheets covered with NiO nanorods may be due to opposite charges as is evident by zeta potential studies (Fig. S1) indicating that the rGO sheets can be used as platform for decoration of nNiO. The decoration of NiO nanorods on rGO surface can be clearly seen from higher resolution images (h) and (i). The image (i) shows a tendency to attach of NiO nanorods with the edges of rGO sheets.

The elemental analysis of nNiO and rGO-NiO was conducted using energy-dispersive X-ray (EDX) analysis. The EDX spectra confirms the existence of Ni (image b) and O_2 elements (Fig. S4, a) in nNiO sample. In spectra (b), the presence carbon due to functional groups in rGO-nNiO matrix. For quantitative EDX analysis, the weight percentage of nickel and oxygen are found to be 80% and 20%, respectively, in nNiO sample (image c). In rGO-NiO, an additional 40% carbon weight percentage appeared due to the functional groups like −OH, C=O, C−O−C, C−O−OH etc. in rGO sample (image d).

Figure 4 shows the transmission electron microscopic (TEM) images of chemically synthesized rGO sheets, nNiO and rGO-NiO composite. The randomly oriented NiO nanorods with low aspect ratio ~5 reveal elongated nanostructure (image a). The high resolution image of NiO nanorods is shown in image (b). The lattice fringes of the nNiO indicates highly crystalline in nature (image c), however, the moire fringes are also seen in nNiO sample. The spacing of lattice fringes for (200) plane is found as 0.20 nm revealing anisotropic growth of the nNiO along (200) direction. In image (d), the rGO planar sheets are observed clearly indicating higher surface-to-volume ratios and morphological 2-dimensional structure of rGO sheets is well maintained. The thick and thin layer of rGO sheets are shown in image (d). With incorporation of rGO sheets, the nNiO decreases their agglomeration (image e) and image (f) shows its high magnification image. In electron diffraction pattern of rGO sheets (inset of image d), two planes (002) and (004) can be observed due to crystalline structure of rGO, which is also supported by the results of the XRD studies.

Electrochemical characterization. The cyclic voltammetric (CV) studies have been conducted on rGO, mesoporous rGO-NiO and after antibodies functionalized electrodes using $[Fe(CN)_6]^{3-/4-}$ as a redox couple at scan rate of 30 mV/s in a potential range of -0.7 to +0.7 V (Fig. 5i). The rGO-based electrode shows well-defined oxidation and reduction peaks due to redox

conversation of $[Fe(CN)_6]^{3-/4-}$ indicating that the electrode follows the Nernst equation. The peak-to-peak potential separation (ΔE) for rGO is estimated as 0.24V for rGO electrode. This potential separation (ΔE) is found to be increases to 0.33 V for mesoporous rGO-NiO electrode. This may be due to positively charged nNiO which can attract more negatively charged electrons from bulk solution.[48] The oxidation current for mesoporous rGO-NiO electrode is found to be several times higher (516 µA) than that of the rGO electrode (118 µA). The nNiO grafting onto rGO sheets improves its electrochemical properties due to its synergistic effect. Liu *et al.* observed that incorporation of the zirconium oxide onto graphene enhanced its electrochemical properties due to fast and reversible redox reactivity.[49] After antibody conjugation with rGO-NiO, current decreases to 388 µA indicating that the antibody immobilized electrode is found to be less conductive compared to rGO-NiO electrode due to inherent insulating properties of antibodies. This confirms that the mesoporous feature of rGO-NiO surface can facilitate the antibody loading *via* covalent interactions. On addition of BSA, the oxidation current decreases due to insulating nature of BSA molecules that block the non-specific sites on electrode surface. Thus, the mesoporous rGO-NiO composite is an ideal material for immunosensing. CV studies of the rGO-NiO based immunoelectrode were conducted as a function of scan rate [10-100 mV/s]. The oxidation peaks are shifted to the positive direction and the reduction peaks potential are shifted to the negative direction with increasing scan rate (Fig. S5). The peaks current are observed to be higher with increased scan rate indicating diffusion controlled process for a redox reaction. The diffusion co-efficient is found to be maximum for mesoporous rGO-NiO electrode (7.9×10^{-5} cm^2/s) compared to rGO electrode (3.77×10^{-6} cm^2/s). However, on AAB and BSA immobilization on rGO-NiO surface decreases the diffusion co-efficient to 4.3×10^{-5} cm^2/s and 2.9×10^{-5} cm^2/s, respectively.

The impedance is a complex resistance encountered when the current flows through resistors and capacitors or inductors circuit. The interfacial properties of electrode such as charge transfer resistance and capacitance can be investigated using this method. The Nyquist plot can be used for quantification of the relative change in charge transfer resistance. The interfacial parameters including R_{ct} (charge transfer resistance) and C_{dl} (double layer capacitance) in Nyquist plot of impedance analysis can be obtained from real (Z') and imaginary $(-Z'')$ impedance as a function of frequencies. The frequency associated with R_{ct} and C_{dl} can be calculated using Eq.3

$$R_{ct}C_{dl} = \frac{1}{2\pi f_{max}} = \tau \quad (3)$$

where, τ is the time constant and f_{max} is the maximum frequency. The potential for impedance measurements was optimized. The observed impedance spectra of rGO-NiO electrode are shown Figure 5ii as a function of potential (0–0.1 V). At low frequency region, the charge transfer resistance of rGO-NiO electrode is found to increase with increasing potential. This indicates that electron transfer kinetics of the redox conversation at low frequency can be controlled by applied potential or polarization potential. Thus, 0.1 V has been optimized for biosensing.

Figure 5iii shows the EIS spectra obtained for various electrodes. A higher value of charge transfer resistance was observed in case of rGO electrode (5 kΩ) compared to rGO-NiO composite electrode (1 kΩ). The available functional groups at rGO perhaps obstruct the electron transfer due to redox conversation resulting in higher impedance signal. On the other hand, nNiO embedded rGO results in improved conduction properties that may introduce electron conduction path for electron transfer from bulk electrolyte solution to ITO electrode resulting in lower impedance signal. Introduction of nNiO on rGO sheets results in improved conductive nature of electrode which may influence the biosensing characteristics. Further, it has been found that the

charge transfer resistance increases on modification of electrode surface by antibody (AAB) and BSA. The AAB on the surface of rGO-NiO electrode forms a protein layer due to strong co-valent interactions, which provide hindrance to the electron transfer from bulk solution leading to higher impedance signal (2 kΩ). The bulky protein BSA further blocks the non-specific site at electrode surface resulting in higher charge transfer resistance. The effect of incubation temperature for immunological reaction between the immobilized AAB on rGO-NiO electrode and LDL molecules has been investigated (Fig. 5iv). The EIS spectra were monitored by varying temperature from 25 to 45 °C at a bias voltage of 0.05V. A maximum response for R_{ct} occurred at an incubation temperature of 25 °C. Thus, an incubation temperature of 25°C to investigate the biosensing performance. The biosensor was tested as a function of pH (4.5 to 8). This biosensor shows a higher charge transfer resistance value at pH 7.0 as shown in Figure S6 and this pH value of PBS solution was chosen for biosensing.

3.7 Low density lipoprotein detection. The impedance of the electrode/solution interface varies when a detectable target analyte is captured by a specific probe. It can thus be utilized to detect the change in impedance signal. The EIS is known to be a label-free operation and it does not require any tagging reagents. The impedimetric response of this label-free biosensor was obtained by varying LDL concentration (0–130 mg/dL) in PBS solution containing $[Fe(CN)_6]^{3-/4-}$ mediator. During Faradic impedance measurements, various concentrations of LDL solution were added into the electrochemical cell at a constant potential (0.1V) and temperature (25 ˚C). The equivalent circuit of the electrochemical impedance system is shown in Fig. 6a (inset). The R_{ct} value (indicates electron-transfer kinetics of redox couple at the electrode interface) of this biosensor is found to increase with increasing LDL concentration [0-130 mg/dL]. At the rGO-NiO electrode surface, a layer formation of LDL molecules due to their specific binding of immobilized AAB may attributed to hinder the generated electrons from redox couple.

A plot between R_{ct} value and LDL concentrations has been shown in Fig. 6b. A calibration plot (Fig. 6b, inset) of R_{ct} value and logarithm of LDL concentration (0-130 mg/dL) is shown in the inset of Figure 6b. The regression equation for this biosensor is $R_{ct}(\Omega)$ = log[0.38] kΩ - log [0.81] kΩ mg^{-1} dL × log [LDL (mg/dL)] with a correlation coefficient of 0.998. The sensitivity of this biosensor is calculated to be as 510 Ω $(mg/dL)^{-1}$ cm^{-2} with a wide detection range of 0-130 mg/dL. The limit of detection (LOD) has been estimated according to IUPAC definition using the $3\sigma_b/m$ criteria, where m is slope of the calibration graph and σ_b is the standard deviation of the blank signal. This fabricated biosensor can be used to detect a low concentration of LDL (LOD: 0.07 mg/dL) compared to other reported biosensors for quantification of LDL molecules [Table S2]. The LOD may be responsible for incorporation of nNiO to rGO sheets which improved the loading capacity of immobilized AAB due to its mesoporous structure for detection of low concentration LDL in PBS. This biosensor can be used to detect higher concentration of LDL (more than 100 mg/dL) after which the sensor response becomes saturated. This biosensor was tested with real serum samples containing LDL molecules by EIS studies as shown in Fig. 6c. With increasing the concentration of LDL in serum, the R_{ct} was found to increase. A comparison plot for real and standard LDL samples is shown in Fig. 6d. The absorption of LDL molecules on the surface of sensor by their specific interaction between antibody-LDL molecules that obstructs the charge transfer from redox reactions in PBS results in enhanced R_{ct}. Table 1 summaries the R_{ct} values obtained for the this biosensor using real and standard LDL concentration with relative standard deviations (RSD). With low RSD's for each concentrations measurements leading to high performance of the rGO-NiO composite in this biosensor. These results indicate that the biosensor can be used to detect LDL concentration in human serum samples in a physiological range of human serum samples (<129 mg/dL).

The LDL molecules contain a hydrophobic core of cholesteryl ester that is coated with phospholipids, cholesterol and apo-protein. The negatively charged LDL molecules (isoelectric

point of LDL is about 5.4 at pH of 7.0) due to coating of phospholipids may repel electrons generated from redox reaction of $[Fe(CN)_6]^{3-/4-}$ resulting in increased the charge transfer resistance. The biosensing characteristics of fabricated rGO-NiO based bioelectrode along with those reported in literature are summarized in Table S2. Figure S7 shows a transient plot for monitoring impedance with detection time in presence of LDL (30 mg/dL) molecules. The impedance is found to be maximum in 100 s, this may be due to that the intrinsic property of mesoporous rGO-NiO composite platform. For stability, the EIS measurements were conducted using the fabricated biosensor in presence of LDL molecules with an interval of 7 days (Fig. 7a and b). Figure 7a shows the overlays of EIS curves and calculated R_{ct} values as a function of number days. The response of this immunosensor decreased to 90.3 % of initial response (R_{ct}) after 35 days. A low RSD (4%, mean=1.69, n=5) of this fabricated biosensor indicates an excellent stability. This may be assigned to strong covalent interactions of AAB on functional mesoporous rGO-NiO composite. The reproducibility studies were conducted by repeating the experiment with four different biosensors that prepared under similar conditions. These electrodes show an average standard deviation of 4% (Fig. 7c). This confirms that a good reproducibility of the biosensor was achievable for the detection of LDL molecules.

To determine selectivity, the effect of analytes including free cholesterol, total cholesterol and triglyceride for this sensor was investigated using EIS technique. The EIS curves and corresponding R_{ct} values are shown in Fig. 8a and b, respectively. With LDL molecules, the biosensor shows a high R_{ct} value as compared to the response of sensor without LDL molecules indicating absorption of LDL molecules on the sensor surface. In presence of the free and total cholesterol molecules, this sensor did not any significant change in its response. However, a minor change (7.1 %) was observed in case of triglyceride molecules. An average standard deviation of 6.5% with exposing different interferents indicates good selectivity of this sensor.

4. Conclusions

We have fabricated a label-free, low cost, reproducible and sensitive biosensor for routine quantification of LDL molecules. A mesoporous defect-less rGO-NiO composite has been utilized to conjugated antibody (AAB) *via* co-valent amide bond (CO-NH) which has been investigated by FT-IR analysis. The spectroscopic Raman mapping studies reveals the confirmation of the defect-less, functionalization and few-layers (about 4-layers) of rGO sheet in synthesized composite. The shape, size and morphology of nNiO and rGO sheets have been studied by electron microscopy. The specific surface area (134.3 m^2/g) of the synthesized rGO-NiO composite by BET analysis and the pore size distribution indicates the presence of mesopores compared to micro and macropores. The rGO sheets provide a suitable platform for the distribution of nNiO which improve the diffusion co-efficient and heterogeneous electron transfer resulting in higher sensitivity and selectivity of this biosensor. This biosensor shows fast detection time (100 s), a lower limit of detection (0.07 mg/dL) and can be used to detect a minute concentration of LDL molecules. The mesoporous structure and available functional groups of rGO in this biosensor shows excellent stability and reproducibility. The efforts should be made to utilize this platform for detection of other biomolecules such as VLDL and cholesterol. This mesoporous rGO-NiO based biosensor has a high potential for the point-of-care diagnostics application.

Supporting Information

Zeta potential investigations for nNiO, rGO sheets, and rGO-NiO composite, thickness measurement of rGO-NiO composite by optical profilometry, UV-visible studies, energy-dispersive X-ray studies for elemental confirmation, scan rate studies for fabricated immunoelectrode, study for biosensor activity at different pH, a transient plot for detection time

with impedance, and tables for pore size distribution from BET data, and comparison of this biosensor with reported literature. This material is available free of charge via the Internet at http://pubs.acs.org.

Notes

The authors declare no competing financial interest.

AUTHOR INFORMATION

Corresponding Authors

*E-mail: ashutos@iitk.ac.in. Tel.: +91 512 259 7026, Fax: +91-5122590104.

#E-mail: bansi.malhotra@gmail.com. Tel.: +91-11-27871043, ext. 1609. Fax: +91-11-27871023.

Acknowledgements

We are thankful to the Department of Science and Technology (DST), New Delhi, India for their support to the Unit on Soft Nanofabrication at Indian Institute of Technology Kanpur. The financial support received from Indian Council of Medical Research, India (Grant No. ICMR/5/3/8/91/GM/2010-RHN) is gratefully acknowledged.

References

1. Kostarelos, K.; Novoselov, K. S., Exploring the Interface of Graphene and Biology. *Science* **2014**, *344*, 261-263.
2. Shao, Y.; Wang, J.; Wu, H.; Liu, J.; Aksay, I. A.; Lin, Y., Graphene Based Electrochemical Sensors and Biosensors: A Review. *Electroanalysis* **2010,** *22*, 1027-1036.
3. Valota, A. T.; Kinloch, I. A.; Novoselov, K. S.; Casiraghi, C.; Eckmann, A.; Hill, E.; Dryfe, R. A. W., Electrochemical Behavior of Monolayer and Bilayer Graphene. *ACS Nano* **2011,** *5*, 8809-8815.

4. Ekiz, O. O.; Urel, M.; Guner, H.; Mizrak, A. K.; Dana, A., Reversible Electrical Reduction and Oxidation of Graphene Oxide. *ACS Nano* **2011**, *5*, 2475-2482.
5. Pumera, M.; Ambrosi, A.; Bonanni, A.; Chng, E. L. K.; Poh, H. L., Graphene for Electrochemical Sensing and Biosensing. *Trends Anal. Chem.* **2010**, *29*, 954-965.
6. Jang, M. S.; Kim, H.; Son, Y.-W.; Atwater, H. A.; III, W. A. G., Graphene Field Effect Transistor Without an Energy Gap. *Proc. Natl. Acad. Sci.* **2013**, *110*, 8786-8789.
7. Liu, S.; Guo, X., Carbon Nanomaterials Field-Effect-Transistor-Based Biosensors. *NPG Asia Mater.* **2012**, *4*, 1-10.
8. Yang, K.; Feng, L.; Shi, X.; Liu, Z., Nano-Graphene in Biomedicine: Theranostic Applications. *Chem. Soc. Rev.* **2013**, *42*, 530--547.
9. Bagri, A.; Mattevi, C.; Acik, M.; J.Chabal, Y.; Chhowalla, M.; Shenoy, V. B., Structural Evolution During the Reduction of Chemically Derived Graphene Oxide. *Nat. Chem.* **2010**, *2*, 581-587.
10. Cui, S.; Pu, H.; Mattson, E. C.; Wen, Z.; Chang, J.; Hou, Y.; Hirschmugl, C. J.; Chen, J., Ultrasensitive Chemical Sensing through Facile Tuning Defects and Functional Groups in Reduced Graphene Oxide. *Anal. Chem.* **2014**, *86*, 7516−7522.
11. Wei, J.; Qiu, J.; Li, L.; Ren, L.; Zhang, X.; Chaudhuri, J.; Wang, S., A Reduced Graphene Oxide Based Electrochemical Biosensor for Tyrosine Detection. *Nanotechnology* **2012,** *23*, 335707.
12. Pumera, M.; Ambrosi, A.; Bonanni, A.; Chng, E. L. K.; Poh, H. L., Graphene for Electrochemical Sensing and Biosensing. *TrAC Trends Anal. Chem.* **2010**, *29*, 954-965.
13. Zhou, M.; Zhai, Y.; Dong, S., Electrochemical Sensing and Biosensing Platform Based on Chemically Reduced Graphene Oxide. *Anal. Chem.* **2009**, *81*, 5603-5613.
14. Kim, Y.; Shanmugam, S., Polyoxometalate−Reduced Graphene Oxide Hybrid Catalyst:Synthesis, Structure, and Electrochemical Properties. *ACS Appl. Mater. Interfaces* **2016**, *5*, 12197-12204.
15. Zhang, W.; Liu, F.; Li, Q.; Shou, Q.; Cheng, J.; Zhang, L.; Nelson, B. J.; Zhang, X., Transition Metal Oxide and Graphene Nanocomposites for High-Performance Electrochemical Capacitors. *Phys. Chem. Chem. Phys.* **2012**, *14*, 16331–16337.
16. Williams, G.; Seger, B.; Kamat, P. V., TiO_2-Graphene Nanocomposites.UV-Assisted Photocatalytic Reduction of Graphene Oxide. *ACS Nano* **2008**, *2*, 1487-1491.

17. Chen, S.; Zhu, J.; Wu, X.; Han, Q.; Wang, X., Graphene Oxide MnO_2 Nanocomposites for Supercapacitors. *ACS Nano* **2010**, *4*, 2822-2830.

18. Zhu, X.; Zhu, Y.; Murali, S.; Stoller, M. D.; Ruoff, R. S., Nanostructured Reduced Graphene Oxide/Fe_2O_3 Composite As a High-Performance Anode Material for Lithium Ion Batteries. *ACS Nano* **2011**, *5*, 3333-3338.

19. Stankovich, S.; Dikin, D. A.; Dommett, G. H. B.; Kohlhaas, K. M.; Zimney, E. J.; Stach, E. A.; Piner, R. D.; Nguyen, S. T.; Ruoff, R. S., Graphene-Based Composite Materials. *Nature* **2006**, *442*, 282-286.

20. Yang, S.; Feng, X.; Ivanovici, S.; Müllen, K., Fabrication of Graphene-Encapsulated Oxide Nanoparticles: Towards High-Performance Anode Materials for Lithium Storage. *Angew Chem. Int. Edit.* **2010**, *49*, 8408-8411.

21. Dutta, S.; Mandal, N.; Bandyopadhyay, D., Paper-based α-amylase detector for point-of-care diagnostics. *Biosen. Bioelectron.* **2016**, *78*, 447-453.

22. Mondal, K.; Ali, M. A.; Srivastava, S.; Malhotra, B. D.; Sharma, A., Electrospun functional micro/nanochannels embedded in porous carbon electrodes for microfluidic biosensing. *Sensor Actuat. B: Chem.* **2016,** *229*, 82-91.

23. Mondal, K.; Ali, M. A.; Agrawal, V. V.; Malhotra, B. D.; Sharma, A., Highly Sensitive Biofunctionalized Mesoporous Electrospun TiO_2 Nanofiber Based Interface for Biosensing. *ACS Appl. Mater. Interfaces* **2014**, *6*, 2516-2527.

24. Ali, M. A.; Mondal, K.; Singh, C.; Dhar Malhotra, B.; Sharma, A., Anti-epidermal growth factor receptor conjugated mesoporous zinc oxide nanofibers for breast cancer diagnostics. *Nanoscale* **2015**, *7*, 7234-7245.

25. Ali, M. A.; Srivastava, S.; Mondal, K.; Chavhan, P. M.; Agrawal, V. V.; John, R.; Sharma, A.; Malhotra, B. D., A surface functionalized nanoporous titania integrated microfluidic biochip. *Nanoscale* **2014,** *6*, 13958-13969.

26. Artiles, M. S.; Rout, C. S.; Fisher, T. S., Graphene-Based Hybrid Materials and Devices for Biosensing. *Adv. Drug. Delivery Rev.* **2011**, *63*, 1352–1360.

27. Lightcap, I. V.; Kosel, T. H.; Kamat, P. V., Anchoring Semiconductor and Metal Nanoparticles on a Two-Dimensional Catalyst Mat. Storing and Shuttling Electrons with Reduced Graphene Oxide. *Nano Lett.* **2010**, *10*, 577-583

28. Gomez-Navarro, C.; Weitz, R. T.; Bittner, A. M.; Scolari, M.; Mews, A.; Burghard, M.; Kern, K., Electronic Transport Properties of Individual Chemically Reduced Graphene Oxide Sheets. *Nano Lett.* **2007**, *7*, 3499-3503.

29. Zhu, J.; Zhu, T.; Zhou, X.; Zhang, Y.; Lou, X. W.; Chen, X.; Zhang, H.; Hng, H. H.; Yan, Q., Facile Synthesis of Metal Oxide/Reduced Graphene Oxide Hybrids with High Lithium Storage Capacity and Stable Cyclability. *Nanoscale* **2011**, *3*, 1084-1089.

30. Kamat, P. V., Graphene-Based Nanoarchitectures. Anchoring Semiconductor and Metal Nanoparticles on a Two-Dimensional Carbon Support. *J. Phys. Chem. Lett.* **2010**, *1*, 520-527.

31. Lang, X.; Hirata, A.; Fujita, T.; Chen, M., Nanoporous Metal/Oxide Hybrid Electrodes for Electrochemical supercapacitors. *Nature Nanotechnol.* **2011**, *6*, 232-236.

32. Williams, G.; Seger, B.; Kamat, P. V., TiO_2-Graphene Nanocomposites. UV-Assisted Photocatalytic Reduction of Graphene Oxide. *ACS Nano* **2008**, *2*, 1487–1491.

33. Wang, C.; Zhou, Y.; Ge, M.; Xu, X.; Zhang, Z.; Jiang, J. Z., Large-Scale Synthesis of SnO2 Nanosheets with High Lithium Storage Capacity. *J. Am. Chem. Soc.* **2010**, *132*, 46–47.

34. Song, J.; Xu, L.; Zhou, C.; Xing, R.; Dai, Q.; Liu, D.; Song, H., Synthesis of Graphene Oxide Based CuO Nanoparticles Composite Electrode for Highly Enhanced Nonenzymatic Glucose Detection. *ACS Appl. Mater. Interfaces* **2013**, *5*, 12928−12934.

35. Jang, H. D.; Kim, S. K.; Chang, H.; Roh, K.-M.; Choi, J.-W.; Huang, J., A Glucose Biosensor Based on TiO_2-Graphene Composite. *Biosen Bioelectron* **2012,** *38* (1), 184-188.

36. Wang, K.; Li, H.-N.; Wu, J.; Ju, C.; Yan, J.-J.; Liu, Q.; Qiu, B., TiO_2-Decorated Graphene Nanohybrids for Fabricating an Amperometric Acetylcholinesterase Biosensor. *Analyst* **2011**, *136*, 3349-3354

37. Wu, M.-S.; Zheng, Y.-R.; Lin, G.-W., Three-Dimensional Carbon Nanotube Networks with a Supported Nickel Oxide Nanonet for High-Performance Supercapacitors. *Chem. Commun.* **2014**, *50*, 8246-8248.

38. Ali, M. A.; Srivastava, S.; Solanki, P. R.; Reddy, V.; Agrawal, V. V.; Kim, C.; John, R.; Malhotra, B. D., Highly Efficient Bienzyme Functionalized Nanocomposite-Based Microfluidics Biosensor Platform for Biomedical Application. *Sci. Rep.* **2013**, *3*, 2661.

39. Liu, S.; Yu, B.; Zhang, T., A Novel Non-Enzymatic Glucose Sensor Based on NiO Hollow Spheres. *Electrochem Acta* **2013**, *102*, 104-107.

40. Solanki, P. R.; Kaushik, A.; Agrawal, V. V.; Malhotra, B. D., Nanostructured Metal Oxide-Based Biosensors. *NPG Asia. Mater.* **2011**, *3*, 17-24.

41. Jayawardena, K. D. G. I.; Rhodes, R.; Gandhi, K. K.; Prabhath, M. R. R.; Dabera, G. D. M. R.; Beliatis, M. J.; Rozanski, L. J.; Henley, S. J.; Silva, S. R. P., Solution processed reduced graphene oxide/metal oxide hybrid electron transport layers for highly efficient polymer solar cells. *J. Mater. Chem. A* **2013,** *1*, 9922-9927.

42. Srivastava, S.; Kumar, V.; Ali, M. A.; Solanki, P. R.; Srivastava, A.; Sumana, G.; Saxena, P. S.; Joshi, A. G.; Malhotra, B. D., Electrophoretically Deposited Reduced Graphene Oxide Platform for Food Toxin Detection. *Nanoscale* **2013**, *5*, 3043-3051.

43. Ali, M. A.; Solanki, P. R.; Patel, M. K.; Dhayani, H.; Agrawal, V. V.; John, R.; Malhotra, B. D., A Highly Efficient Microfluidic Nano Biochip Based on Nanostructured Nickel Oxide. *Nanoscale* **2013**, *5*, 2883-2891.

44. Mondal, K.; Kumar, J.; Sharma, A., Self-organized macroporous thin carbon films for supported metal catalysis. *Colloid Surface A: Physicochem. Eng. Aspect.* **2013,** *427*, 83-94.

45. Katiyar, S.; Mondal, K.; Sharma, A., One-step sol-gel synthesis of hierarchically porous, flow-through carbon/silica monoliths. *RSC Adv.* **2016**, *6*, 12298-12310.

46. Wang, H.; Wang, Y.; Cao, X.; Feng, M.; Lan, G., Vibrational Properties of Graphene and Graphene Layers. *J. Raman Spectrosc.* **2009**, *40*, 1791–1796.

47. Zhong, L.; Yun, K., Graphene oxide-modified ZnO particles: synthesis, characterization, and antibacterial properties. *Int. J. Nanomedicine* **2015**, *10*, 79-92.

48. Solanki, P. R.; Ali, M. A.; Agrawal, V. V.; Srivastava, A. K.; Kotnala, R. K.; Malhotra, B. D., Highly sensitive biofunctionalized nickel oxide nanowires for nanobiosensing applications. *RSC Adv.* **2013**, *3*, 16060-16067.

49. Liu, J.; Meng, X.; Hu, Y.; Geng, D.; Banis, M. N.; Cai, M.; Li, R.; Sun, X., Controlled Synthesis of Zirconium Oxide on Graphene Nanosheets by Atomic Layer Deposition and Its Growth Mechanism. *Carbon* **2013**, *52*, 74-82.

Figures

Schematic 1. The functionalization of rGO-NiO composite with antibody for detection of low density lipoprotein.

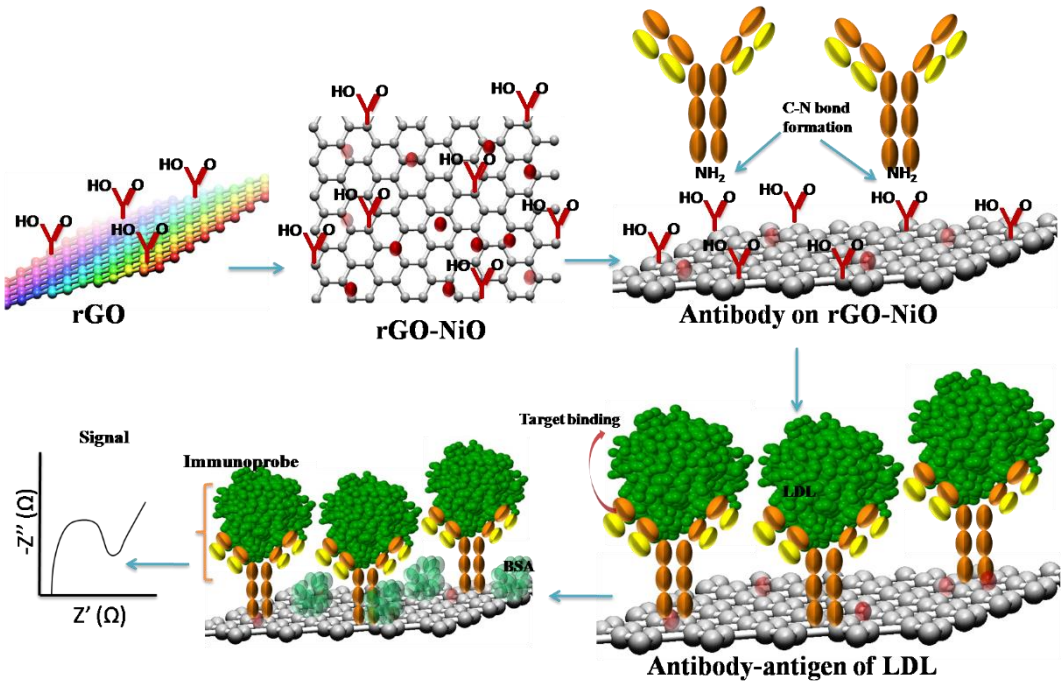

Figure 1 The N_2 adsorption and desorption isotherms of rGO-NiO, inset shows the pore size distribution curve of rGO-NiO composite (a), Raman (b) and FT-IR (c) studies of fabricated films and XRD studies of rGO and rGO-NiO composite (d).

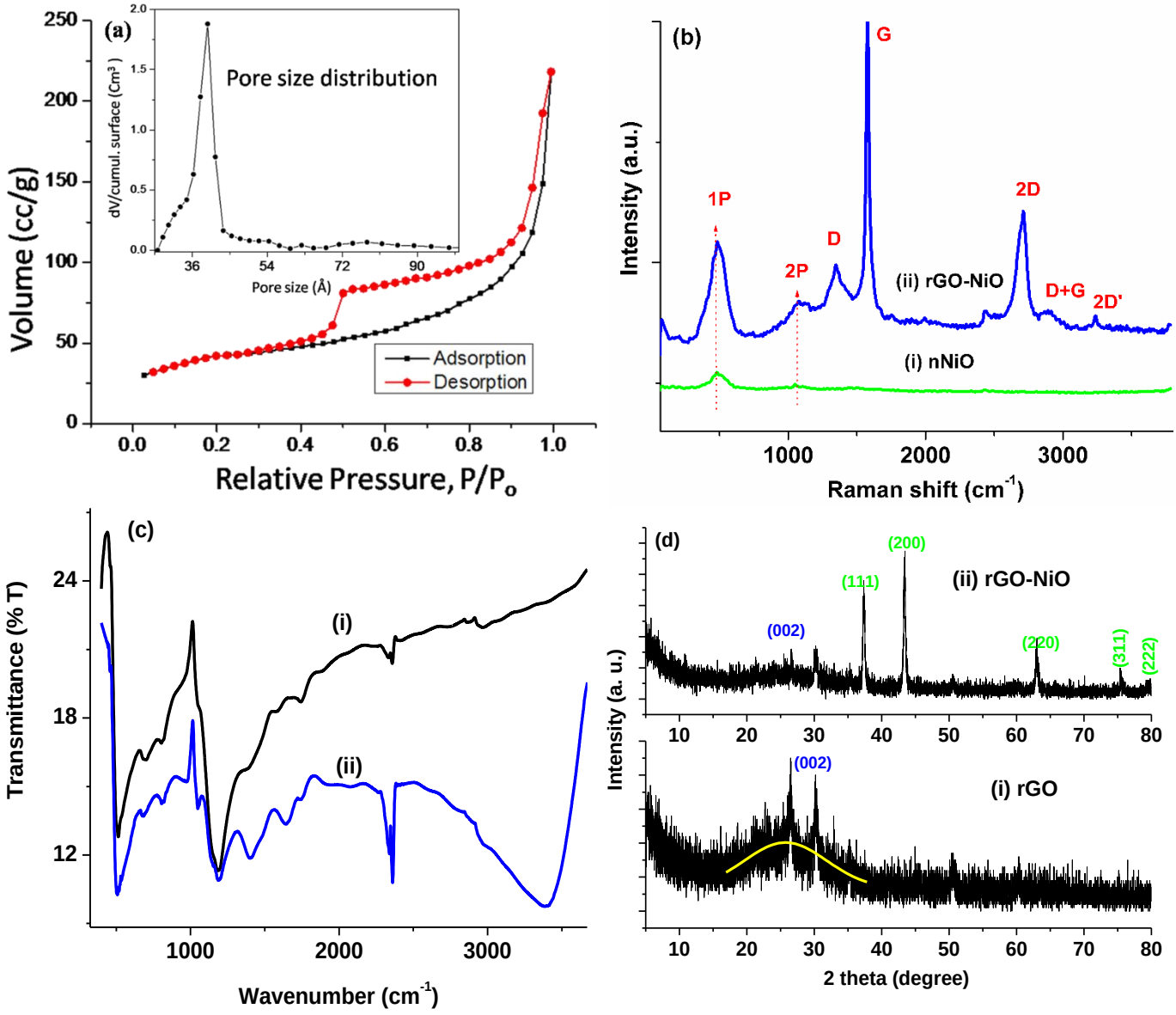

Figure 2 Spectroscopic Raman mapping rGO-NiO composite. Image (a) is simple optical micrograph of nNiO with rGO sheets and (b) the colourful intensity image of various peaks (D, G, and 2D). (c) 2D and (d) 3D optical profilometric image of rGO-NiO composite.

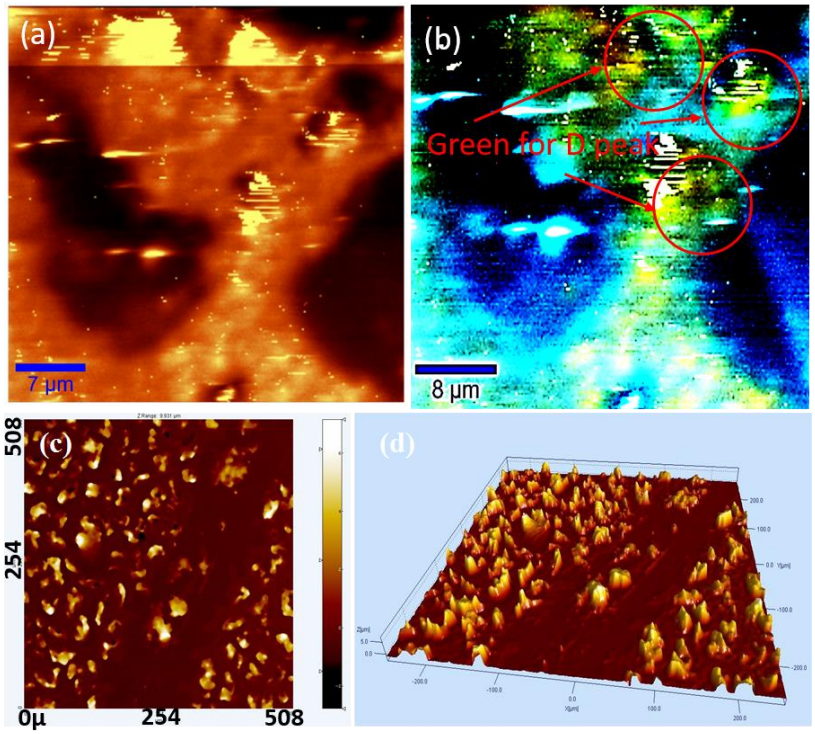

Figure 3 FESEM images of NiO nanorods (a and b), FESEM image of rGO sheets (c, d and e), rGO-NiO composite (f and g), and high resolution image of rGO-NiO composite (h and i).

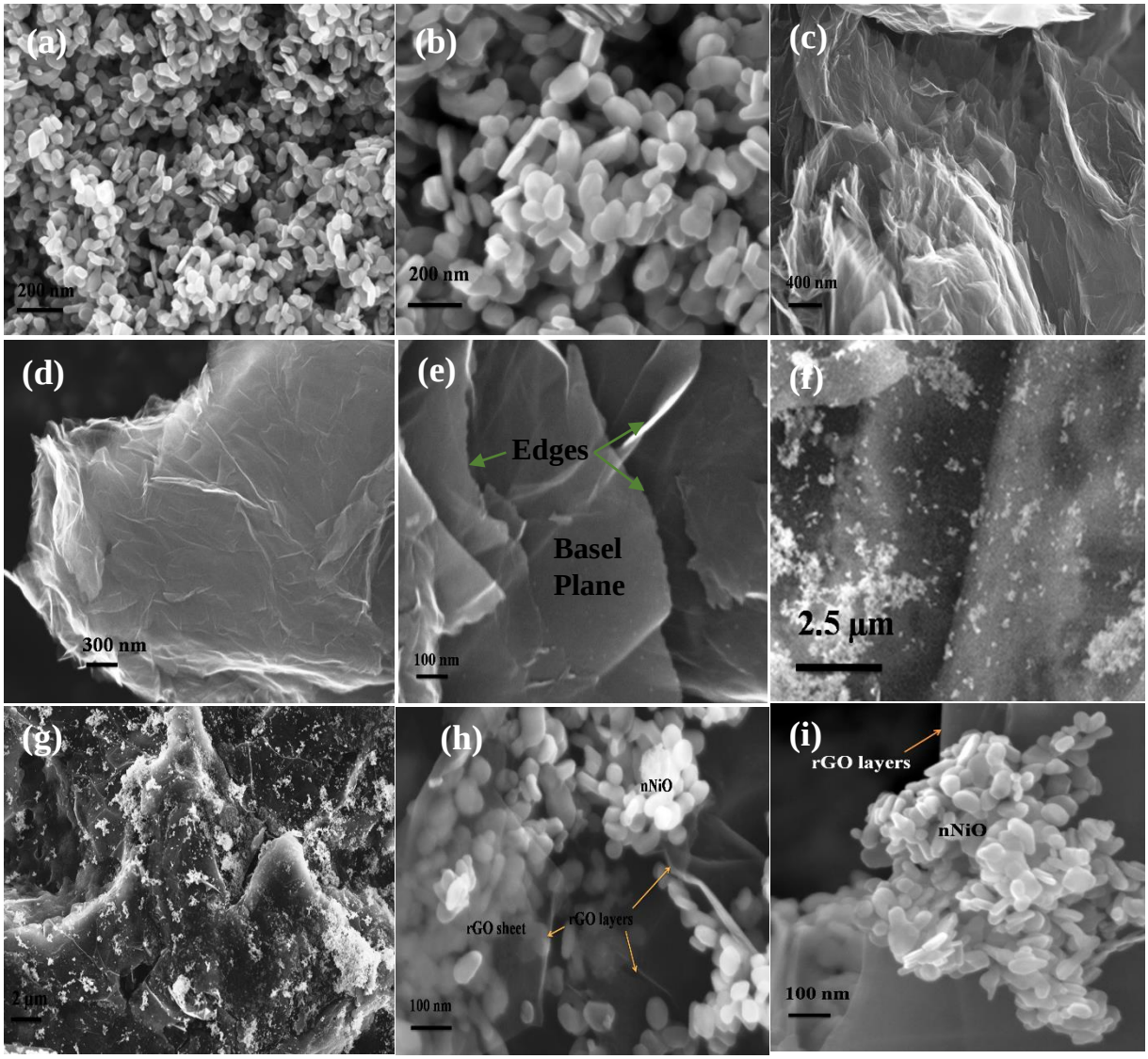

Figure 4 TEM images of NiO nanorods (a and b), atomic scale image of NiO nanorods (c), TEM image of rGO sheets (d), inset of (d) showing selected area electron diffraction pattern of rGO, rGO-NiO composite (e), and higher resolution image of rGO-NiO composite (f).

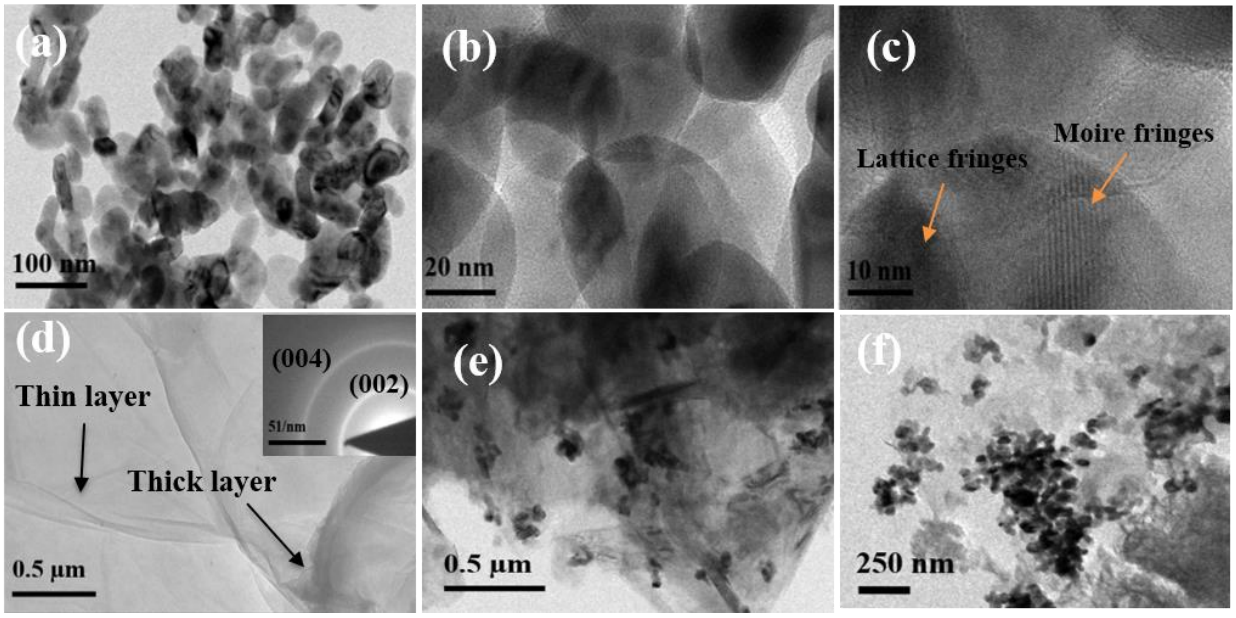

Figure 5 CV of various electrodes at 30 mV/s in PBS at pH 7.0 containing 5 mM of $[Fe(CN)_6]^{3-/4-}$ as a redox species (i), EIS spectra of rGO-NiO electrode as a function of potential (ii), EIS measurements of various fabricated electrodes (iii) and EIS spectra of rGO-NiO based bioelectrode as a function of temperature (iv).

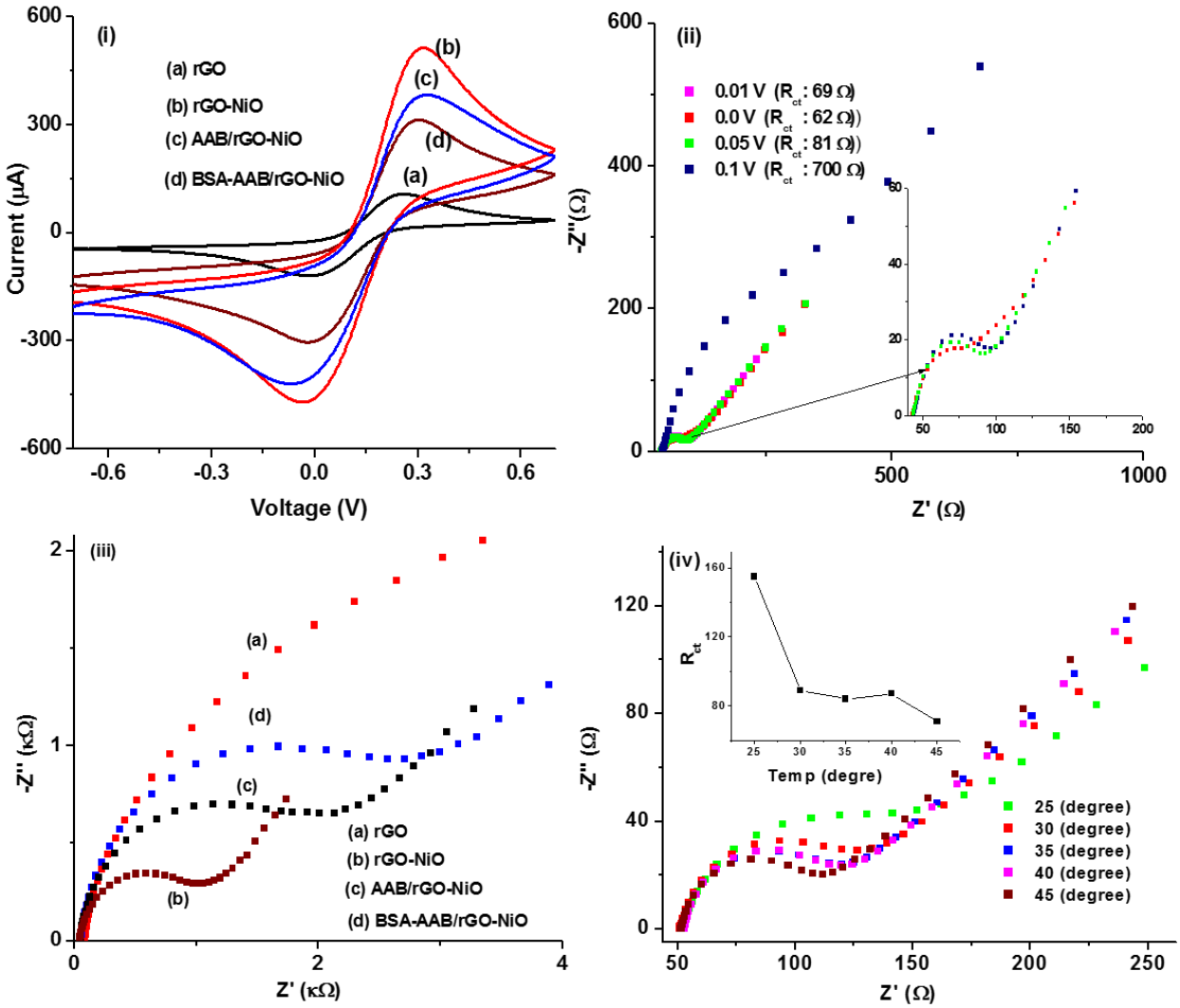

Figure 6. EIS response study of the biosensor as a function of LDL concentration at 0.1 V (a) and the plot between the R_{ct} value and LDL concentration (b), inset shows its logarithm plot of sensor calibration. (c) EIS response of fabricated biosensor as a function of LDL concentration 5-130 mg/dL in blood serum samples and (c) comparison plots of the R_{ct} values with LDL concentrations for real and standard samples.

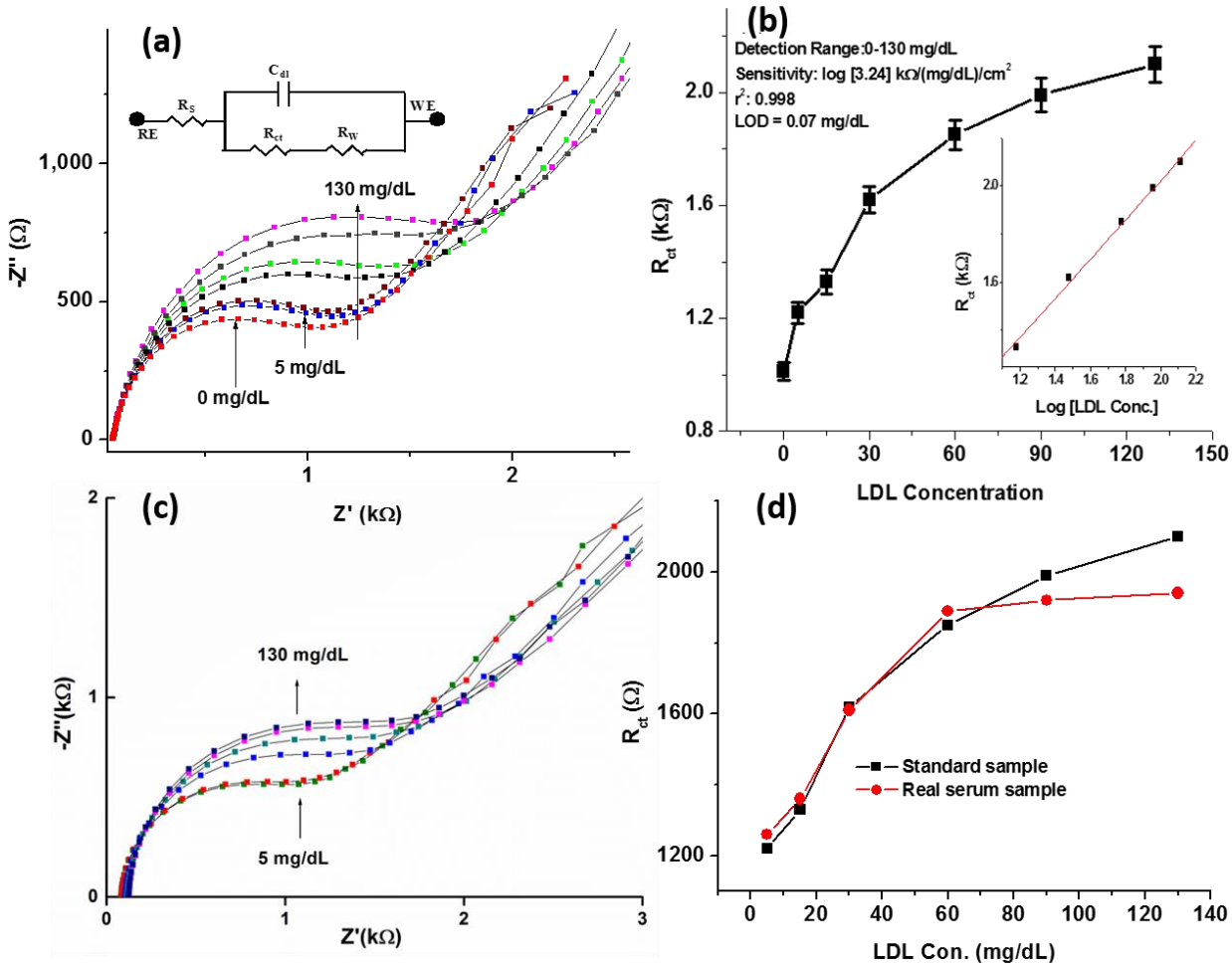

Figure 7. (a) The fabricated immunosensor has been tested for 35 days and electrochemical impedance spectra in presence of LDL molecules (60 mg/dL) and (b) the plot between obtained R_{ct} values verses number of days. (c) The plot for immunosensors responses with number repeated electrodes.

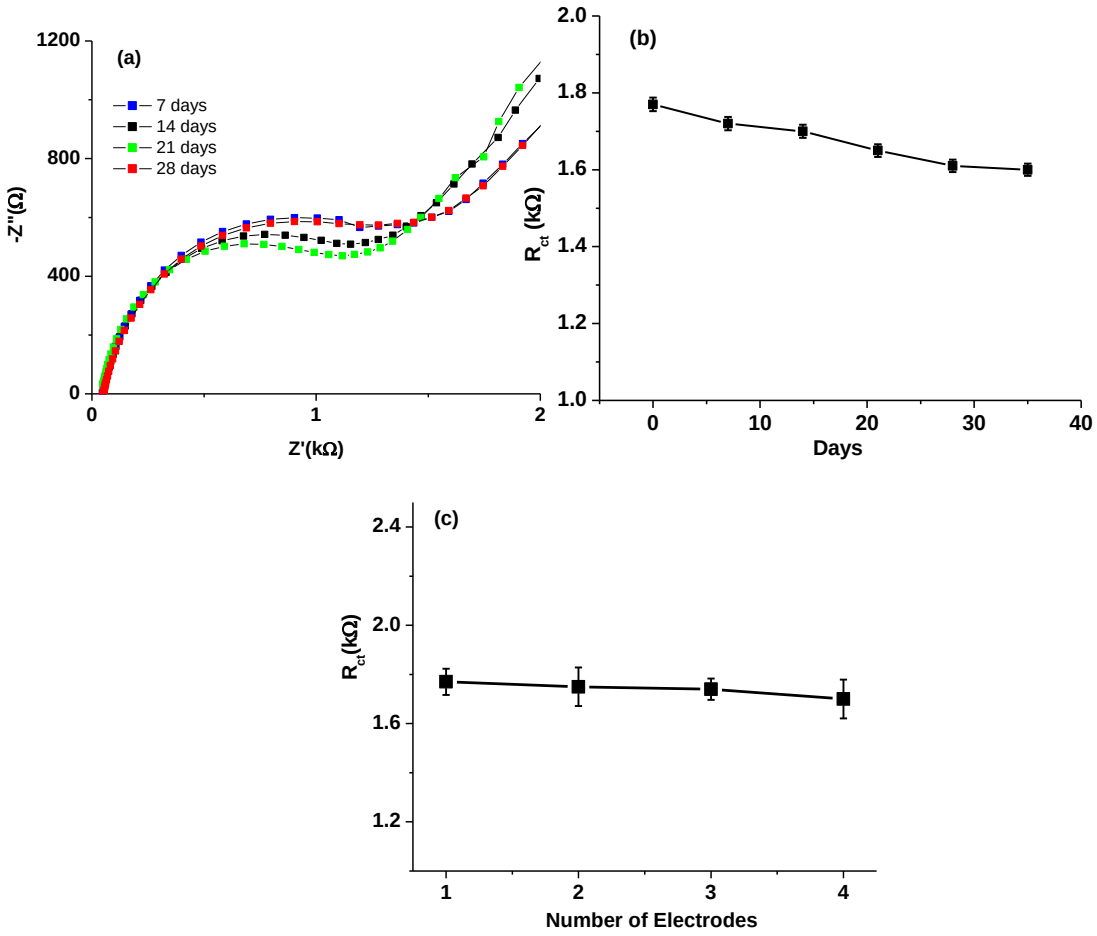

Figure 8. (a) The EIS spectra for selectivity studies of the fabricated biosensor. The concentration of free cholesterol, total cholesterol, and triglyceride were set to 150 mg/dL. These interfering molecules were mixed with 90 mg/dL of LDL molecules. (b) Corresponding R_{ct} values plot with different interferents.

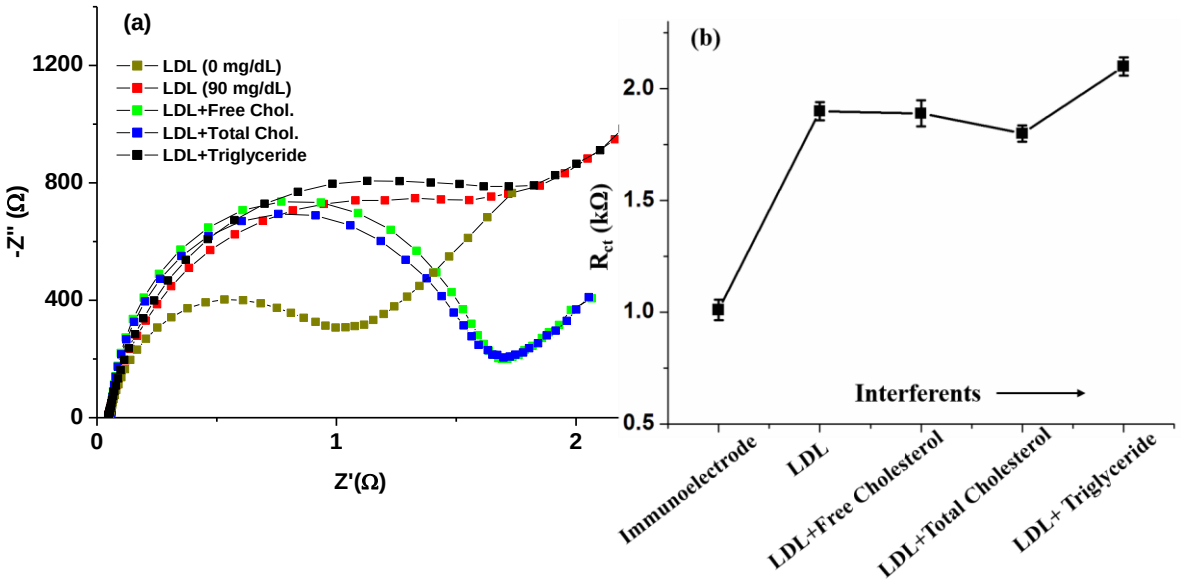

Table 1. The sensor performances for quantification of real and standard LDL concentrations.

LDL concentration (mg/dL)	Value of R_{ct} obtained with standard solution (Ω)	Value of R_{ct} obtained with serum sample (Ω)	% RSD
5	1220	1260	2.28
15	1330	1360	1.58
30	1620	1610	0.44
60	1850	1890	1.51
90	1990	1920	2.90
130	2100	1940	5.60

Graphical Abstract